Remote Sensing of Environment 187 (2016) 49–61

Contents lists available at ScienceDirect

Remote Sensing of Environment

journal homepage: www.elsevier.com/locate/rse

Detecting seasonal landslide movement within the Cascade landslide complex (Washington) using time-series SAR imagery

Xie Hu [a], Teng Wang [a], Thomas C. Pierson [b], Zhong Lu [a,*], Jinwoo Kim [a], Thomas H. Cecere [c]

[a] Huffington Department of Earth Sciences, Southern Methodist University, Dallas, TX, USA
[b] U. S. Geological Survey, Vancouver, WA, USA
[c] U. S. Geological Survey, Reston, VA, USA

ARTICLE INFO

Article history:
Received 20 May 2016
Received in revised form 17 September 2016
Accepted 2 October 2016
Available online xxxx

Keywords:
Cascade landslide complex
Columbia Gorge landslides
Time-series amplitude analysis
Time-series interferometric synthetic aperture radar (InSAR) analysis
Seasonal landslide movement
Precipitation-correlated landslide motion
Precipitation triggers
Landslide kinematics

ABSTRACT

Detection of slow or limited landslide movement within broad areas of forested terrain has long been problematic, particularly for the Cascade landslide complex (Washington) located along the Columbia River Gorge. Although parts of the landslide complex have been found reactivated in recent years, the timing and magnitude of motion have not been systematically monitored or interpreted. Here we apply novel time-series strategies to study the spatial distribution and temporal behavior of the landslide movement between 2007 and 2011 using InSAR images from two overlapping L-band ALOS PALSAR-1 satellite tracks. Our results show that the reactivated part has moved approximately 700 mm downslope during the 4-year observation period, while other parts of the landslide complex have generally remained stable. However, we also detect about 300 mm of seasonal downslope creep in a terrain block upslope of the Cascade landslide complex—terrain previously thought to be stable. The temporal oscillation of the seasonal movement can be correlated with precipitation, implying that seasonal movement here is hydrology-driven. The seasonal movement also has a frequency similar to GPS-derived regional ground oscillations due to mass loading by stored rainfall and subsequent rebound but with much smaller magnitude, suggesting different hydrological loading effects. From the time-series amplitude information on terrain upslope of the headscarp, we also re-evaluate the incipient motion related to the 2008 Greenleaf Basin rock avalanche, not previously recognized by traditional SAR/InSAR methods. The approach used in this study can be used to identify active landslides in forested terrain, to track the seasonal movement of landslides, and to identify previously unknown landslide hazards.

© 2016 Elsevier Inc. All rights reserved.

1. Introduction

Landslides are slope failures in response to the increased ratio of destabilizing shear stress to resisting shear strength. They are generally recognized as the physical responses to external triggers: heavy rainfall or rapid snowmelt (increased pore-pressure) [e.g., Iverson, 2000], ground shaking (earthquakes and volcanic eruptions) [e.g., Malamud et al., 2004], ecologic events (wildfires) [e.g., Cannon et al., 2001], atmospheric tides [e.g., Schulz et al., 2009], and anthropogenic activities (overdevelopment, mining, and deforestation) [e.g., Highland and Bobrowsky, 2008]. However, the recent extreme landslides in Oso, WA in 2014 [Iverson et al., 2015; Kim et al., 2015] and in Nepal following the 2015 earthquake [Kargel et al., 2016] escalated the need to identify potential catastrophic sliding hazards in mountainous regions and to further assess the associated risks.

Detection of slow or limited landslide movement within broad areas of forested terrain has long been problematic, because slide motion may not disturb the forest enough to make the slides easily visible, and even if slide locations are known, traditional ground-based methods of landslide monitoring are difficult to use in remote areas. Since the early 1990s, Interferometric Synthetic Aperture Radar (InSAR) techniques have measured cm- to mm-level deformation in various geodynamic settings [e.g., Simons and Rosen, 2007]. With the capability of surveying large areas, both during day and night, SAR techniques have proven very useful for detecting and mapping large landslides in the northwestern USA [Zhao et al., 2012]. InSAR methods can provide critical information on landslide location, boundaries, and movement [e.g., Hilley et al., 2004; Calabro et al., 2010; Zhao et al., 2012; Kim et al., 2015]. In this work, we apply time-series InSAR techniques to two adjacent tracks of L-band ALOS PALSAR-1 images acquired between 2007 and 2011, to systematically investigate the spatial distribution and temporal behavior of movement within the Cascade landslide complex and adjacent terrain.

1.1. Geological setting of the Cascade landside complex

Landslides are common in the Columbia River Gorge due to steep slopes and heavy seasonal rainfall. In the western part of the Gorge,

* Corresponding author.
E-mail address: zhonglu@smu.edu (Z. Lu).

http://dx.doi.org/10.1016/j.rse.2016.10.006
0034-4257/© 2016 Elsevier Inc. All rights reserved.

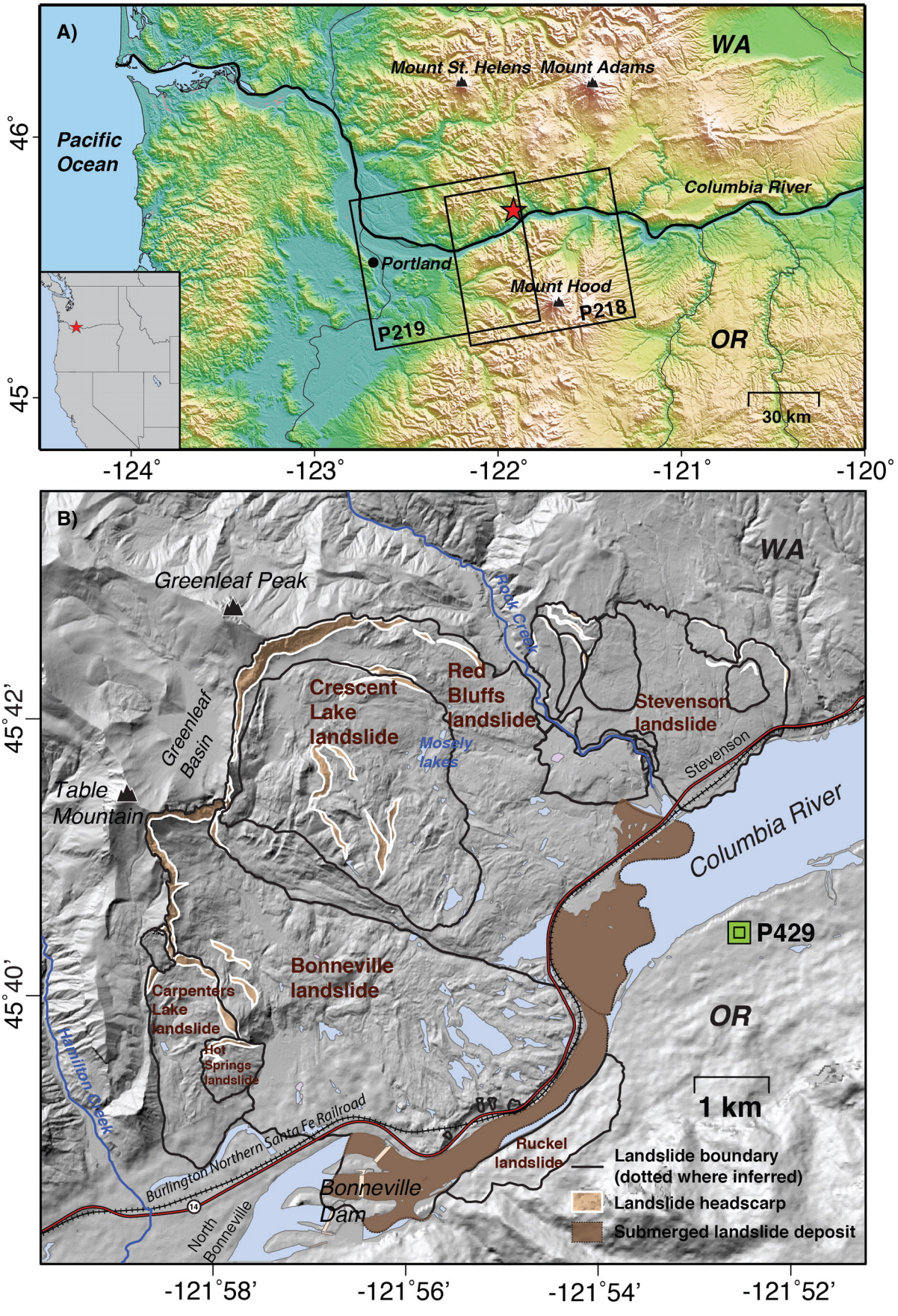
A)
WA
Mount St. Helens
Mount Adams
Pacific Ocean
Columbia River
Portland
Mount Hood
P218
P219
OR
30 km
46°
45°
-124°
-123°
-122°
-121°
-120°
B)
WA
Greenleaf Peak
Rock Creek
Red Bluffs landslide
Crescent Lake landslide
Stevenson landslide
Mosely lakes
Greenleaf Basin
Stevenson
Table Mountain
Columbia River
P429
Bonneville landslide
Carpenters Lake landslide
Hot Springs landslide
OR
Hamilton Creek
1 km
Burlington Northern Santa Fe Railroad
Ruckel landslide
Landslide boundary (dotted where inferred)
Bonneville Dam
Landslide headscarp
North Bonneville
Submerged landslide deposit
45°42'
45°40'
-121°58'
-121°56'
-121°54'
-121°52'

landslides occur predominantly on the Washington side of the river, owing to the composition and structure of the underlying bedrock [Palmer, 1977; Pierson et al., 2016]. Four landslides within the ~36-km^2 Cascade landslide complex in Skamania County, Washington have been active within the last 600 years and one is currently active. For this reason, it is a significant site for potential future hazards. The Cascade landslide complex (Fig. 1) was originally mapped as four landslides: Carpenters landslide, Bonneville landslide, Red Bluffs landslide, and Mosley Lakes landslide [Wise, 1961]. More recent mapping [Randall, 2012] has shown that what was thought to be the Mosley Lakes landslide was only a part of the Red Bluffs landslide. However, another part of the Red Bluffs landslide has reactivated within the last few decades, and is now mapped as the Crescent Lake landslide [Pierson and Lu, 2009; Pierson et al., 2016]. Immediately east of the Cascade landslide complex is the newly recognized Stevenson landslide [Randall, 2012; Pierson et al., 2016], which is occupied by the City of Stevenson (population ~1500). Monitoring the movement of the landslides in this area is important due to their potential threats to the residents, roads, and infrastructure, which includes a natural gas pipeline, high-voltage electric transmission lines, a major rail line, a commercial navigation channel in the river, two large tourist facilities, and Bonneville Dam.

The Cascade landslide complex occurs within a gently dipping sequence of weak, chemically altered volcaniclastic sedimentary rocks and minor interbedded lava flows that are overlain by more competent layers of rock [Wise, 1961; Walsh et al., 1987; Pierson et al., 2016]. The underlying sediments are principally volcaniclastic sandstones and conglomerates of intermediate composition that range from Oligocene to early Miocene in age. The volcaniclastic units are capped by an originally thick sequence of more competent rock composed of Miocene flood basalts, late Miocene-to-Pliocene fluvial deposits, and localized Quaternary mafic lavas. The failure planes of these dominantly translational landslides occur in bedding-parallel, clay-rich weak zones within the volcaniclastic sediments that dip from 2° to 10° southward toward the river.

1.2. Landslide history within the Cascade landslide complex

Landslides in the western Columbia River Gorge have been occurring for at least tens to hundreds of thousands of years, but the landslides in the Cascade landslide complex are all <600 years old [Pierson et al., 2016]. The Bonneville landslide broke off from terrain near Table Mountain in the early 15th century and filled the Columbia Gorge with about 1 km^3 of debris, dammed the river for a period of at least months, and formed a natural "bridge" across the Gorge that gave birth to the Native American legend of the Bridge of the Gods [Lawrence and Lawrence, 1958; Palmer, 1977; O'Connor, 2004, 2009; Pierson et al., 2016] (Fig. 1 B). After the natural dam was breached, the river channel was displaced about 1 km to the south. Morphologic features of the Carpenters Lake and Red Bluffs landslides suggest that they are both younger than the Bonneville landslide, and a radiocarbon date from the toe of the Red Bluffs landslide suggests that it could be as much as 200 to 300 years younger than the Bonneville landslide [Pierson et al., 2016]. Furthermore, reactivated parts of the Carpenters Lake and Red Bluffs landslides have been active within the last 20 years—the Hot Springs and Crescent Lake landslides, and at least the latter is currently active [Pierson and Lu, 2009; Tong and Schmidt, 2014; Schmidt and Tong, 2015]. In addition, the Greenleaf Basin rock avalanche (about 375,000 m^3—small in comparison to the other landslides making up the Cascade landslide complex) broke off from the western side of the headscarp of the Red Bluffs landslide on January 3, 2008 [Randall, 2012].

1.3. Landslide monitoring methods

Classic methods of landslide monitoring include both ground-based motion- and distance-detection sensors and the analysis of remote sensing imagery [Gili et al., 2000]. In-situ landslide monitoring utilizes classical surveying methods and ground-based sensors, e.g., Global Positioning System (GPS), borehole inclinometers, strain gauges, and rock noise instruments; however, they are spatially limited, labor-intensive, costly, and technically challenging. Aerial remote sensing imageries are also useful for landslide monitoring, but pre- and/or post-slide images are not always practically available at small scale, and the image quality is heavily dependent on the condition of atmospheric water vapor, the extent of vegetative coverage, and the existence of identifiable features.

Under inclement weather conditions, SAR imagery may be the only effective method for detection of unmapped landslides and monitoring active sliding motion in remote regions [e.g., Zhao et al., 2012]. However, monitoring landslide-induced deformation using InSAR has been limited by the following aspects. First, InSAR-based monitoring typically involves the inconsistency of scattering centers (the 3-D position of the dominant scatterer who occupies the strongest electromagnetic echo within the pixel) between radar echoes and various Digital Elevation Model (DEM) data sources, such as Shuttle Radar Topography Mission (SRTM) and Light Detection And Ranging (LIDAR), as a result of different wavelengths of the electromagnetic waves. Second, InSAR measurements can be contaminated by atmospheric water vapor. And third, landslide movement may be non-linear in time. To overcome these limitations, specific strategies for time-series InSAR analysis need to be designed.

In this study, we focus on the spatial extent and temporal behavior of the landslide motion by applying specifically designed time-series InSAR analysis. We obtained time-series deformation by suppressing decorrelation-related sources, such as topographic errors (topo-errors) and atmospheric artifacts, and quantified the kinematics of the active landslides. We used SAR datasets from two adjacent and overlapping satellite tracks to cross-validate our results. The comparison of our InSAR measurements with regional deformation observed by GPS and meteorological records further allows us to better understand landslide behavior in response to precipitation, which is relevant to the possible occurrence of future landslides.

2. Methodology

2.1. Data preparation

We collected two overlapping ascending tracks of L-band ALOS PALSAR-1 SAR data acquired between 2007 and 2011: 24 acquisitions of Path 218 (P218) from June 2007 to February 2011 and 15 acquisitions of Path 219 (P219) from February 2007 to October 2010. Since the launch ALOS PALSAR-1 in May 2006, its perpendicular baseline (the distance perpendicular to the radar line-of-sight (LOS) direction between two satellite passes) was increasing quasi-linearly during the first 2 years. Then an orbital maneuver was performed in July 2008 with an abrupt ~7000 m baseline shift. Significant topo-errors in the interferograms can be expected with large perpendicular baselines [Samsonov, 2010]. To avoid the incorrect phase estimations due to a large baseline,

Fig. 1. Cascade Landslide Complex. (A) Segments of ascending ALOS PALSAR satellite tracks from Path 218 (P218) and Path 219 (P219) (black boxes), superimposed on the shaded relief map. Three major volcanic centers (black triangles)—Mount St. Helens and Mount Adams on the Washington side and Mount Hood on the Oregon side—surround the Cascade landslide complex (red star). The inset is a sketch map of western USA. (B) Shaded-relief map of Cascade landslide complex, composed of Carpenters Lake landslide (including the reactivated Hot Springs landslide), Bonneville landslide, Red Bluff landslide (including the reactivated Crescent Lake landslide), and the newly recognized Stevenson landslide adjacent to the east [Pierson et al., 2016]. Green square indicates the location of GPS station P429. Landslide outlines are from Pierson et al. [2016]. (For interpretation of the references to color in this figure legend, the reader is referred to the web version of this article.)

a common strategy for time-series analysis of ALOS PALSAR-1 datasets is to avoid using data acquired during the summer of 2008 [e.g., Handwerger et al., 2015], which normally results in a disconnected baseline network. From pre-generated interferograms, we estimated that the localized movement along LOS in the sliding body may exceed half of the L-band ALOS's wavelength, i.e., ~12 cm, during one single wet season from November to the following February. To best construct the connected baseline network, we first divided the datasets into two groups for each track according to their acquisition time – one prior to and the other after the satellite orbital maneuver. For the preliminary interferometric pair selection, our strategy is to extract data pairs with perpendicular baselines within 1300 m and temporal intervals within 540 days, in addition to using only data pairs acquired during one wet season. Next, to bridge the gap caused by the orbital maneuver in mid-2008, several interferograms involving two wet seasons were chosen (unwrapping interferograms including three or more wet seasons is unresolvable in the study area). After culling out the contaminated data pairs with low coherence, we obtained 42 interferograms for P218 and 28 interferograms for P219 (Fig. 2).

We also processed C-band ENVISAT ASAR data, however, it is difficult maintain coherence with large deformation gradients, fine-grained landslide debris and thick vegetation cover that occur in the study area.

2.2. Interferometric processing

Localized large movement and heavy vegetation in the Cascade landslide complex lead to difficulty in phase unwrapping. We therefore needed to carefully consider the number of looks and the window size of the filters applied to interferograms. A larger number of looks reduces phase noise but at the cost of lower resolution. Larger window size of the filters smooths the intensive fringes but may cause loss of detail at fringe boundaries. The trade-off between the number of looks and the ability to reveal detail is especially important in areas with a large deformation gradient, such as the currently active Crescent Lake landslide. In our study, we applied 4 looks in range (i.e., ~30 m ground range pixel spacing) and 8 looks in azimuth (i.e., ~25 m azimuth pixel spacing). Interferograms were generated using GAMMA software.

Long-wavelength ionosphere noise is influential at high latitude and over a large-scale region. Our study area is localized (~40 km^2) at the latitude of ~45.66°, and we find the ionosphere noise is ignorable compared with other main sources of artifacts such as topographic error, orbital ramps, and atmospheric water vapor delay. We applied a polynomial function to estimate the orbital ramps based on the unwrapped interferograms processed by the GAMMA minimum-cost-flow module. Although quadratic or higher-level polynomial functions fit better with the phase map, higher-level functions may introduce high-order ramp anomalies, especially for the poorly correlated interferograms with sparse credible measurements. Hence, for each selected interferometric pair, we applied a linear polynomial function using the input of pixels with coherence larger than 0.6. In addition, we ensured that these pixels were not located in areas with potential motion, such as the slide body and the active stratovolcanoes, i.e., Mount St. Helens, Mount Adams and Mount Hood (black triangles in Fig. 1 A). The derived polynomial coefficients were used to estimate the orbital ramps, which were then subtracted from the original wrapped interferograms, and the remainders were used in the following time-series InSAR analysis.

2.3. Time-series InSAR analysis

In order to retrieve the temporal behavior of landslide motion, we carried out time-series InSAR analysis based on unwrapped interferograms. Our processing can be divided into three sections (Fig. 3): coherent target (CT) detection, topographic error (topo-error) removal and atmospheric phase screen (APS) removal.

2.3.1. Coherent target (CT) selection

CTs are defined as pixels with high coherence and stable amplitude series in time. To separate CTs from water bodies, vegetated areas, and other sources with inconsistent scattering, we set thresholds on coherence and dispersion of amplitude (DA, the ratio between the standard deviation and the mean of the amplitude). The pixels with DA < 0.35, averaged coherence larger than 0.8, and each pixel with an individual coherence larger than 0.3 is chosen as a CT (Fig. 6 A for P218 and Fig. 6 B for P219). The scarcity of CTs on the lower part of the Bonneville landslide deposit for both P218 and P219 can be explained by the existence of many lakes and dense forest vegetation. Because our study area is located on the far range of P219 swath (no data are available from P219 beyond this eastern boundary), the satellite antenna received backscattering with a lower signal-to-noise-ratio for this zone, thereby reducing the interferometric coherence. Hence, the CT points in P219 are even sparser than those in P218.

To achieve spatial consistency for each interferogram, we set up a reference where we assume no deformation during the observation period. The phase value of a few reference points might be contaminated by the atmosphere during some acquisitions, thereby further biasing the measurements of all connected interferometric pairs. Therefore, we selected the CT points at two independent residential areas of North Bonneville and Stevenson (Fig. 1 B) as the reference, where the

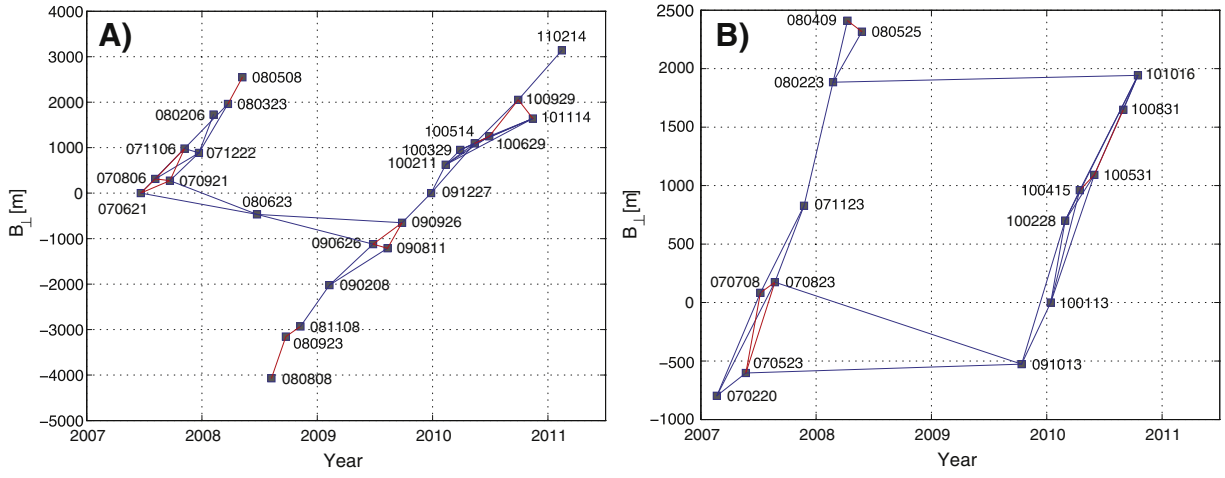

Fig. 2. Baseline network of interferograms from P218 (A) and P219 (B) datasets. Y-axis shows the perpendicular baseline in meters. The imagery acquisition dates are represented in the format of YYMMDD. All the connecting lines represent interferometric pairs used for time-series analysis. Red connecting lines are interferometric pairs with temporal intervals <92 days in dry seasons that are used for topographic error estimation. (For interpretation of the references to color in this figure legend, the reader is referred to the web version of this article.)

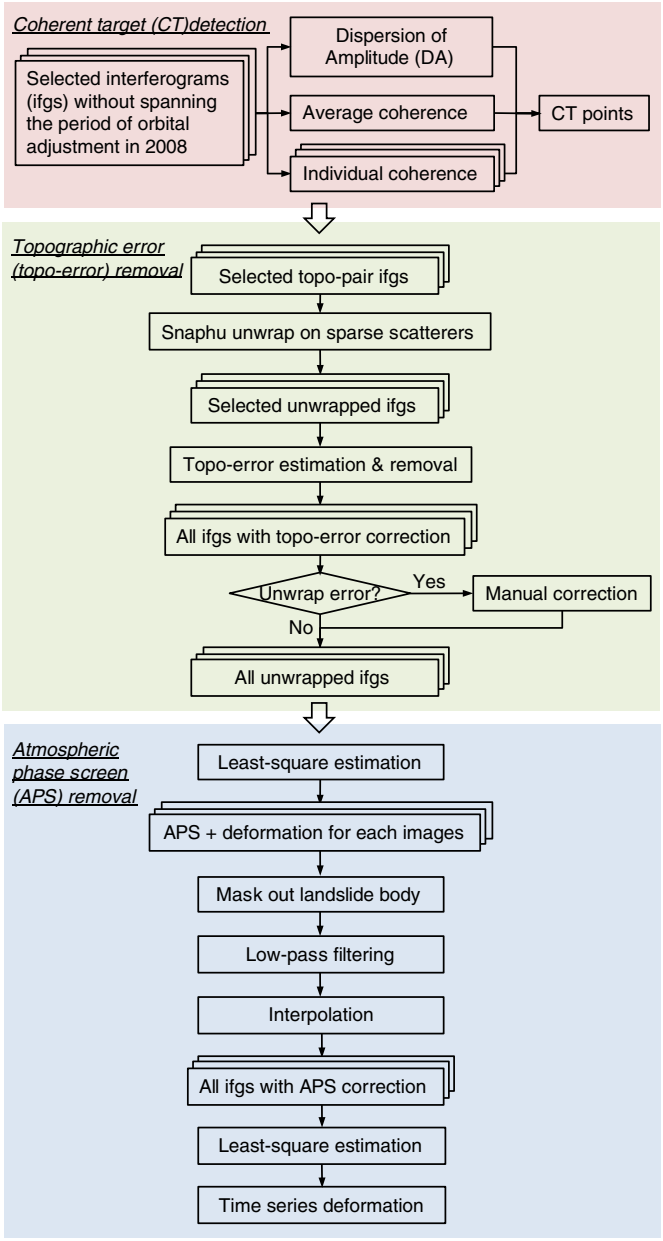

Fig. 3. Workflow of time-series InSAR processing.

coherence is good and the interferograms do not show fringes, and subtracted their averaged phase value from that of all CT points. Note that all the following data processing is based on those discrete CT points.

2.3.2. Topographic error (topo-error) removal

To remove the topographic phase component from each interferogram, a 10-m-posting DEM was generated by using a 5-m-resolution LIDAR bare-earth DEM [DNR, 2005] and filling out the remaining area with a 30-m-resolution SRTM DEM to best utilize the available DEM resources. The systematic error was corrected by minimizing the elevation difference of the overlapping regions (Fig. 4 A). However, the two DEMs are still inconsistent with a large elevation difference (Fig. 4 A and B). Interestingly, the DEM difference map seems to reflect the distribution of forest vegetation, suggesting that the origin of this inconsistency may be explained by the sensors' different sensitivities to the vegetated terrain and the resulting difference in scatterer center height. SRTM used C-band radar data acquired in 2000, which is sometimes incapable of fully penetrating the tree crown in dense canopy (Fig. 5). Therefore, SRTM-derived elevation could be situated at a level between canopy and ground surface containing (partial) tree height. On the other hand, LIDAR DEM corresponds to the bare-earth elevation in 2005. The misfits between two DEM sources can vary from pixel to pixel, and the effects are more notable in vegetated terrain. Most commonly, the differences in acquisition time, scattering centers, and the volumetric scattering effects, as well as the inaccuracy of geocoding and coregistration, contribute to such inconsistency.

The elevation difference between the SRTM and LIDAR DEMs represents their different scattering centers, but neither of the DEMs can precisely reflect the actual scattering center of the L-band ALOS data for our time-series InSAR processing. We therefore need to estimate the topo-errors before the investigation of deformation signal. We first selected the interferograms (Fig. 2) with temporal intervals within 92 days (i.e., two orbital cycles for ALOS data) in dry seasons for which we assumed no deformation. Then we conducted Snaphu unwrapping on sparse CT points [Chen and Zebker, 2001; Hooper, 2010], and estimated the topo-errors by analyzing the time-series unwrapped phase behavior with respect to the perpendicular baseline for each CT point. We encountered difficulty with phase unwrapping some decorrelated interferograms (e.g., the bridging data pairs of P219); in those cases, we performed manual correction by adding or subtracting an integer number of phase cycle(s) at the phase discontinuity.

Our topo-error estimations from the P218 and P219 datasets are shown in Fig. 4 C. Interestingly, the localized bluish area at the toe of the Bonneville landslide, which is only covered by the SRTM DEM, corresponds to a clear-cut area. Historic aerial images show that the logging activities have been ongoing for decades. Without topo-error correction, the fringes will result in spurious subsidence signals, as the temporal and spatial baselines are correlated for ALOS data (Fig. 2) [Samsonov, 2010]. Similar phenomena also exist in other logged areas covered only by the SRTM DEM to the east side (out of the boundary) of our study area. On the other hand, the reddish area close to the north tip of Bonneville landslide, where we used the LIDAR DEM, corresponds to a vegetated hillslope facing east. Without topo-error correction, our estimation can be contaminated by spurious uplift signals. We removed the derived topo-error phase component on each CT from all the interferograms before phase unwrapping.

2.3.3. Atmospheric phase screen (APS) removal

Based on the unwrapped interferograms, we used least-square estimation (LSE) to derive time-series deformation for each point, and applied the coherence as a weighting function during the inversion. However, the deformation signals here are likely to be contaminated by APS with low frequency in the spatial domain. Hence, we masked out the landslide body and conducted low-pass filtering (linear interpolation) in space to extract the APS signals. Based on the APS estimated on the remaining scatterers, we can apply an interpolation method (e.g., the Kriging interpolation) to interpolate APS on all the PSs for each acquisition [Ferretti et al., 2001]. After removing the APS from each interferogram and applying additional LSE, we obtained the time-series deformation map.

3. Results

3.1. Characterization of initial movement of the Greenleaf Basin rock avalanche

The Greenleaf Basin rock avalanche was reported to have occurred at the headscarp conjunction of the Red Bluffs and Bonneville landslides on January 3, 2008 [Randall, 2012]. Nevertheless, the phase information cannot be utilized to detect this rock avalanche because of the complete loss of coherence. Instead, we extracted the scatterers along the flow path of the avalanche in areas with relatively large amplitude dispersion

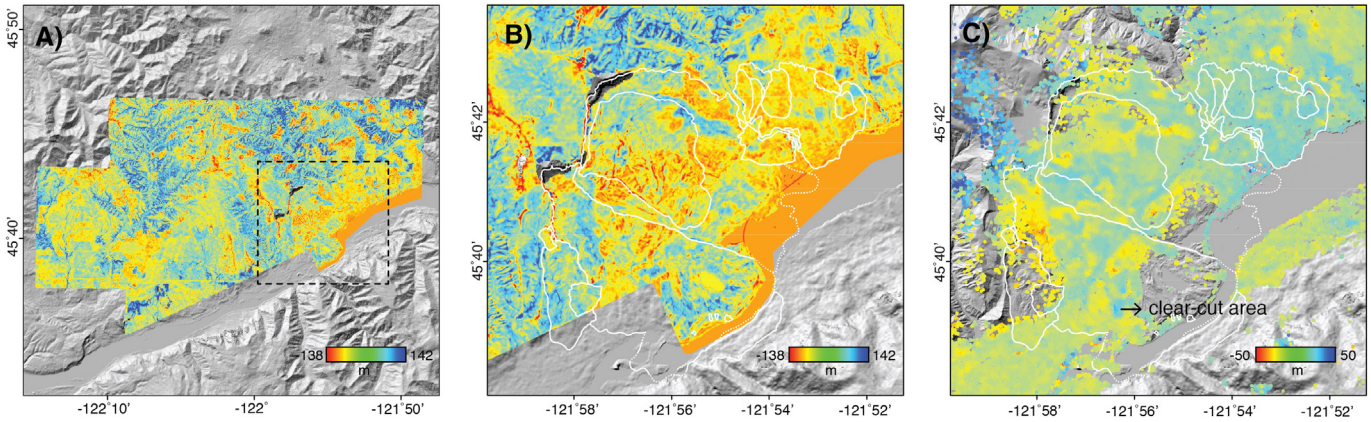

Fig. 4. Sources of topographic error in the analyses. The elevation difference map between SRTM DEM and LIDAR DEM over the DEMs overlapping area (A) and the study area (B). The study area is outlined by the dashed box in A. The color scales in A and B show the elevation difference in meters. (C) Topographic error of the merged DEM estimated by P218 and P219 datasets with respect to the merged LIDAR and SRTM DEMs. The color scale in C shows the topographic error in meters. (For interpretation of the references to color in this figure legend, the reader is referred to the web version of this article.)

(DA > 1). The averaged time-series amplitude values of both P218 and P219 datasets on those scatterers show a sudden drop by ~15 decibel (dB) at the end of 2007, which may suggest the fractures might have initiated between November 23, 2007 and December 22, 2007, close to a month earlier than the reported date of rapid collapse on January 3, 2008.

3.2. Spatial pattern of sliding motion of the Crescent Lake landslide

The landslide motion of the Crescent Lake landslide can be successfully detected using our InSAR processing strategy after DEM and atmospheric artifacts have been reduced. Fig. 6 A and B show the time-series deformation along the radar LOS, as estimated from two independent datasets P218 and P219. Although the radar geometry of these two datasets differs by 2°, the temporal and spatial movement patterns are generally consistent. In general, there is subtle ground movement (~1–2 cm along LOS) in dry seasons, and the landslide moves the most (>10 cm along LOS) during the wet seasons from November to February with a precipitation greater than ~50 cm [Randall, 2012]. The motion is not spatially uniform within the landslide; the zone of greatest movement is in the upper and northeastern parts of the landslide. This movement has formed a steep-fronted landslide toe that terminates just upslope of the Mosely Lakes (Fig. 1 B and Fig. 6).

Detectable ground motion also extends into the Greenleaf Basin upslope of the Red Bluffs landslide headscarp (Fig. 6)—terrain that had previously been assumed to be stable. This could be the incipient

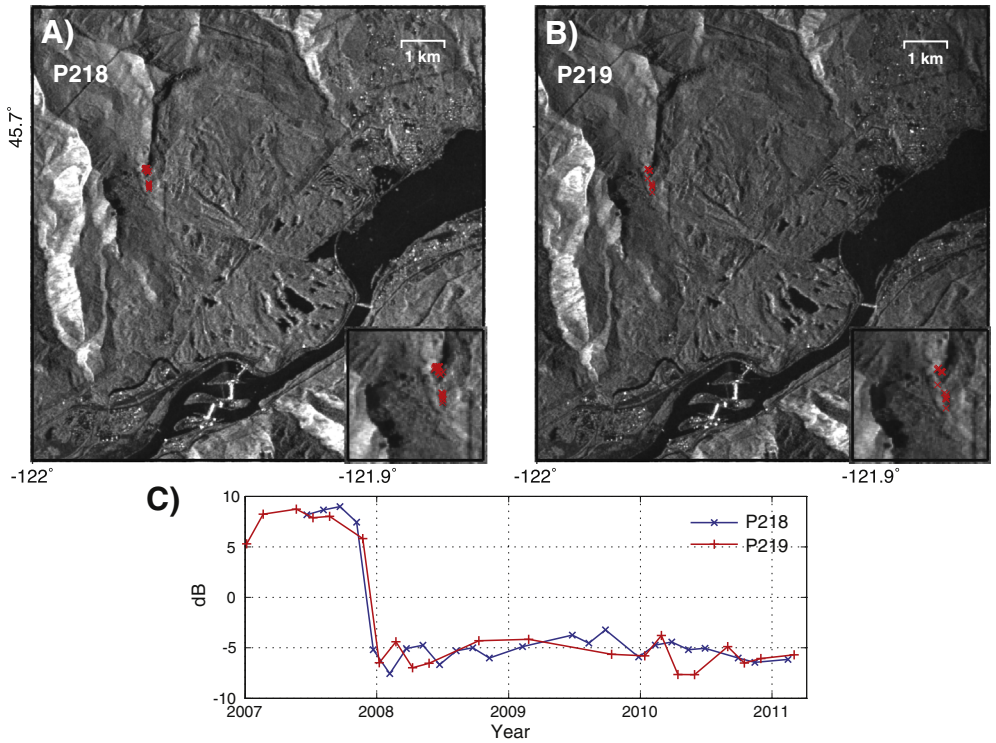

Fig. 5. Detection of the Greenleaf Basin rock avalanche. Averaged amplitude image of P218 (A) and P219 (B) datasets. Red "X"s indicate pixels with dispersion of amplitude larger than 1, consistent with the reported location of the Greenleaf Basin rock avalanche. Insets show the enlarged view of selected pixels. (C) Averaged time-series amplitude of those selected pixels. (For interpretation of the references to color in this figure legend, the reader is referred to the web version of this article.)

movement leading to another rock avalanche. Our results show that the moving area is >0.8 km^2 with an averaged cumulative LOS movement of around 200 mm, corresponding to approximately 300 mm slope-parallel movement from 2007 to 2011, and the movement mainly occurred during the wet seasons. Notably, the basin terrains relatively far from the headscarp show larger magnitude of movement than the near field, suggesting the bulk of the rock fragments may break away from a new segment in the basin, rather than along the existent headscarp like the 2008 rock avalanche. The potential avalanche could perhaps involve as much as 100 million m^3, which could possibly reach important infrastructure downslope.

The deformation map derived from interferograms allows us relocate parts of the Crescent Lake landslide boundaries as defined by surface morphology [Pierson et al., 2016]. Namely, the northeast and southwest boundaries should be stepped back ~150 m southwestward. Furthermore, the clear deformation discontinuity on the boundary between the Crescent Lake and Bonneville landslides, combined with the compressional morphologic features indicated from the hillshading (Fig. 1 B) suggest two independent and resisting basal planes for these two slides. In contrast to the Crescent Lake landslide, coherent parts of Red Bluffs, Bonneville and Stevenson landslides have remained stable during the observation period. The activity of the Hot Springs landslide

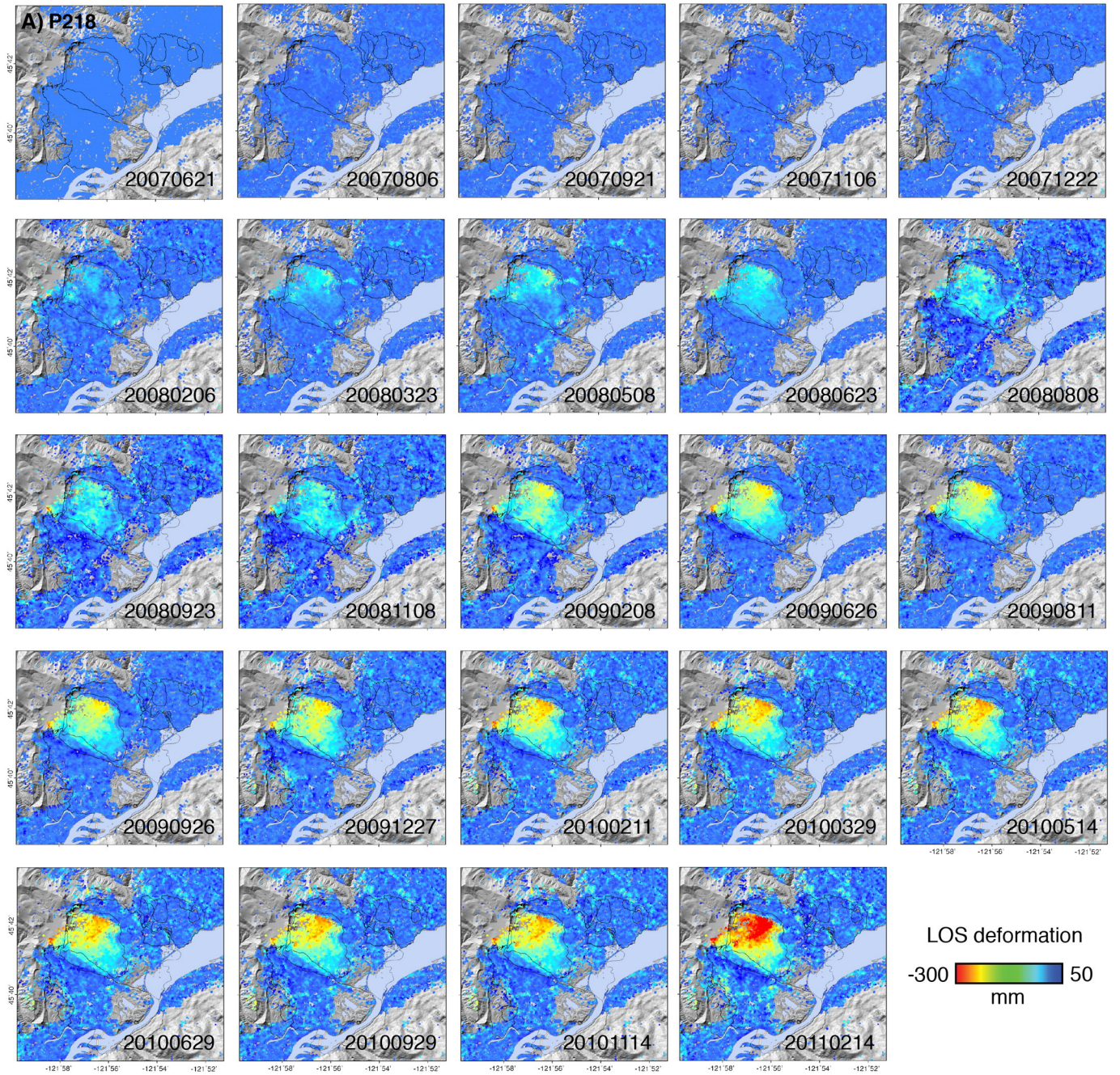

Fig. 6. Time-series deformation along radar line-of-sight (LOS) from satellite track P218 between June 21, 2007 and February 14, 2011 (in A) and from satellite track P219 between February 20, 2007 and October 16, 2010 (in B). The color scale shows LOS deformation in millimeters, with areas having no deformation shown in color blue. Our study area is located near the central range of P218, yet at very far range of P219. No data are available from P219 beyond this eastern boundary. The signal-to-noise ratio is lower at the far range than the central range, and thus lower interferometric coherence, resulting in a sparser CTs distribution of P219. All results are calibrated to the first acquisition on February 20, 2007. (For interpretation of the references to color in this figure legend, the reader is referred to the web version of this article.)

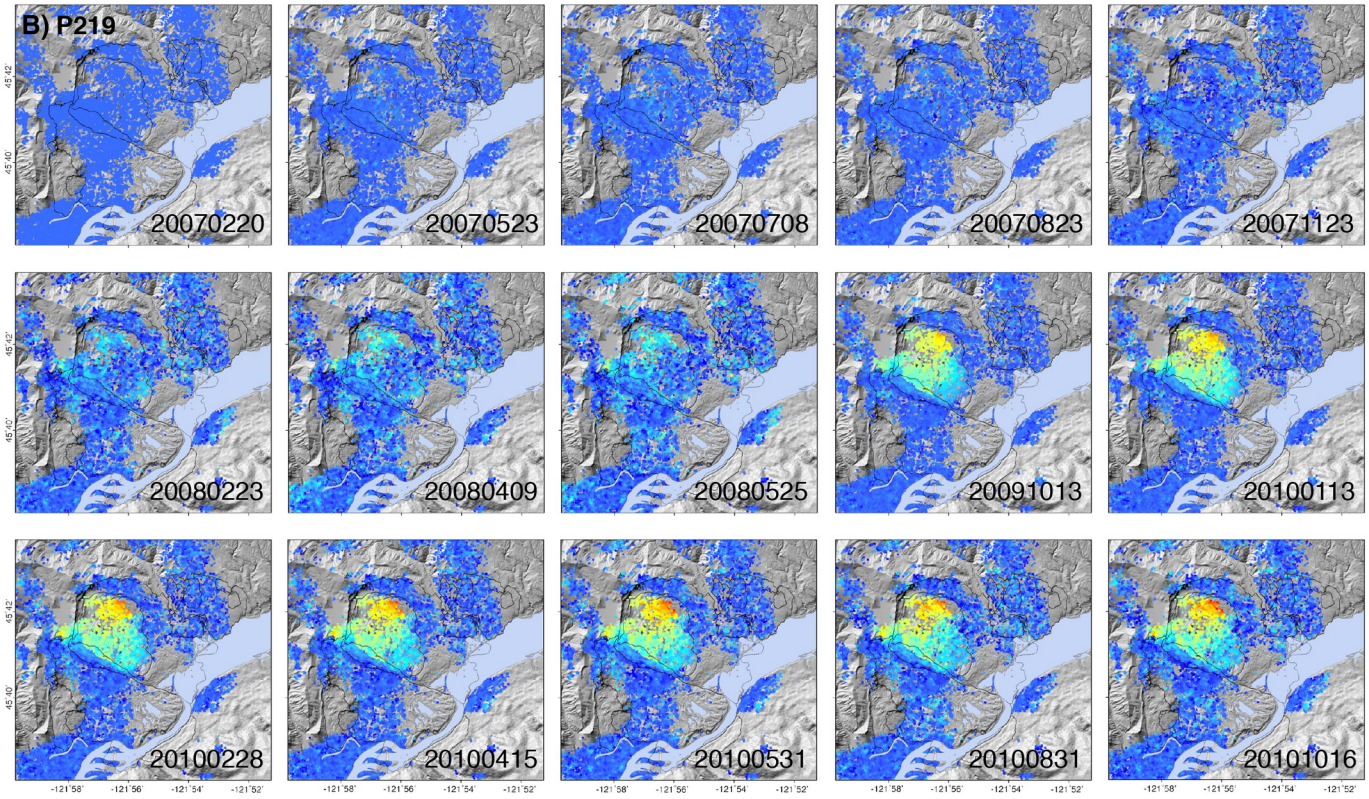

Fig. 6 (*continued*).

and the remaining part of Carpenters Lake landslide are still undetermined due to a lack of CTs.

3.3. Slope-parallel movement of Cascade landslide complex

InSAR can only measure the projection of the 3-dimensional ground motion along radar LOS direction while the actual sliding is generally in the slope-parallel direction. Landslides in the Cascade landslide complex are dominantly translational landslides [Palmer, 1977; Pierson et al., 2016]. For translational landslides, we can assume that the landslide basal failure planes and the surface slope are approximately parallel, so that the projection of the slope-parallel vector on the horizontal plane can be referred to as the slope aspect. Fig. 7 A illustrates two general situations given smooth slopes: one is on the slope facing the incoming radar pulses, the downslope motion corresponds to the slant range decrease; the other is on the slope facing away from the incoming radar pulses, the downslope motion corresponds to the slant range increase. In both cases, the magnitude of downslope sliding vector is always no less than that of the radar look vector. This amplification/scaling factor A of the LOS measurement when projected into the hillslope can be expressed as $A = 1/(l \cdot s^T)$ [Hilley et al., 2004], where l is the radar look direction unit vector $l = [-\sin\varphi_{look}\sin\alpha_{head} \quad \sin\varphi_{look}\cos\alpha_{head} \quad -\cos\varphi_{look}]$, and s is the downslope sliding unit vector $s = [\cos\sigma_{slp}\cos\beta_{asp} \quad \cos\sigma_{slp}\sin\beta_{asp} \quad -\sin\sigma_{slp}]$, in which φ_{look} is the radar look angle, α_{head} is the radar heading angle, σ_{slp} is the slope angle, and β_{asp} is the slope aspect, α_{head} and β_{asp} are positive when rotating clockwise from the north/zero orientation (Fig. 7 B and C).

Generally, slopes in the Columbia Gorge directly face the Columbia River. Thus the two opposite river banks have opposite aspects (Fig. 8 A). In our study region, the slope aspects reflect a divergent fan pattern from the main upland area toward the river, resulting in the angle between the aspect vector and radar look vector ranging from acute to obtuse, and therefore, the amplification factor can be either positive or negative (Fig. 8 B). When this angle reaches 90°, i.e. the radar look vector and slope are perpendicular to each other, the absolute value of amplification will result in an invalid infinite number. Therefore, the amplification factors are especially undetermined around the areas of transition from blue to red, such as along Rock Creek (Fig. 1 B), the sharp topographic relief in between the east-facing slope (deep blue), and the area of deep red within the Bonneville landslide.

Our study area is located in the middle range of P218, but it is on the far range of the P219 swath. Thus, the radar look vectors for the same ground target in the P218 and P219 datasets are slightly different, but the slope-parallel vectors are identical. This results in different amplification values. At location *P* for example (Fig. 8 D), the incidence angle is 38.16° for P218 and 40.53° for P219, resulting in an amplification of 1.69 for P218 and 1.63 for P219. Given the same downslope movement of 100 mm, the corresponding LOS movement will be 59 mm for P218 and 61 mm for P219.

Fig. 8 C and D show the cumulative LOS movement from P218 and the derived slope-parallel movement after applying the amplification correction pixel by pixel. Considering the possible divergence between the failure plane aspect and the surface slope aspect at any given points within the landslide, the surface slope aspect may not always point to the direction of sliding, which can lead to inaccurate amplification factors. To control the large deviations of slope-parallel movement estimations, we culled out isolated pixels with absolute amplification value larger than a certain threshold (e.g., 5) to facilitate the interpretation. Consequently, the number of CT points in Figs. 8 C and D is less than that shown in Fig. 8 B. Nevertheless, the slope-parallel movement allows us to better identify the sliding body and improve the quantification of real motion. Besides the change in movement magnitude, the overall movement pattern after applying amplification also looks different from that of LOS measurements. Apart from the active area on the

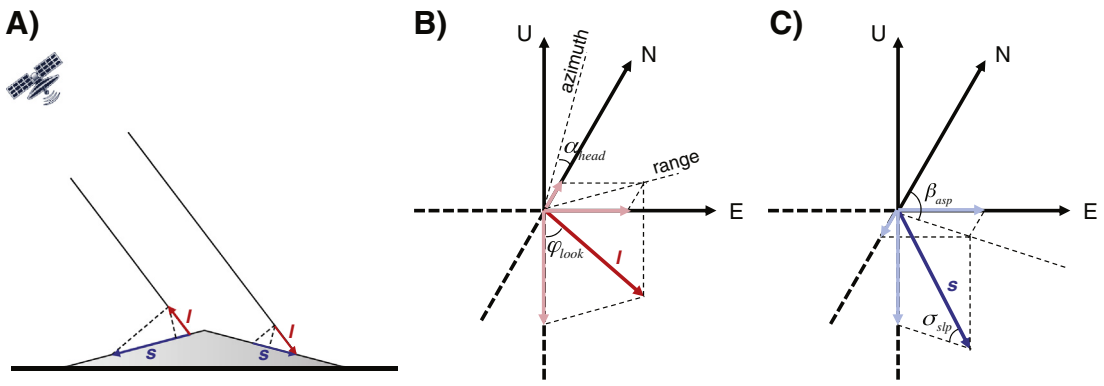

Fig. 7. Implications of radar look angles. (A) Lateral view of the projection of radar look vector *l* into slope-parallel vector *s*. Projection corrections for (B) radar look vector and (C) slope-parallel vector in 3-D space. The vectors are defined by the left-handed Cartesian coordinate system, where north, east and up directions are x, y and z axes respectively, and clockwise rotation from the axes indicates an increase in the angles.

upper NE lobe of the Crescent Lake landslide, we see another area concentrated with increased movement in the upper SW part of the Crescent Lake landslide. The slope-parallel movement map suggests similar amount of total movement for the two areas.

3.4. Seasonal deformation in response to precipitation

An advantage of data from ALOS PALSAR-1 satellite passes occurring every 46 days is that correlations between landslide movement and the amount and timing of precipitation can be performed. We used singular value decomposition (SVD) [Berardino et al., 2002] to integrate time-series deformation measurements of the P218 and P219 datasets. An example at point *P* (Fig. 8 D) is shown in Fig. 9, and the results from those two independent satellite tracks have good consistency. This active area is consistently moving away from the satellite between 2007 and 2011. The cumulative movement of 400 mm along LOS converts to as much as 700 mm movement along the slope. The increased InSAR temporal sampling made possible by integrating these two tracks will allow us to better explore landslide behavior in response to rainfall.

We obtained the daily precipitation records at Bonneville Dam meteorological station, which span the entire SAR observation period. The temporal intervals of ALOS satellite passes ranged from 17 to 138 days with an average of around 40 days. To synchronize the temporal resolution of precipitation and SAR observations, we compared the slope-parallel motions with the 30-day accumulated precipitation total preceding the acquisition date (Fig. 9 B). To investigate the seasonal kinemics of the landslide system, we removed the linear component (black dash line in Fig. 9 A) from the original InSAR-derived motion history. The positive values in Fig. 9 B mean the motion magnitude falls above the linear regression; similarly, the negative values mean the motion magnitude falls below the linear regression. The time-series deformation demonstrates clear seasonal variation, and it has a strong correlation with the quasi-periodic 30-day accumulated precipitation total (Fig. 9 B). During the wet seasons, sufficient precipitation infiltrates and saturates the ground in the basal part of the landslide body. This saturation likely elevates the pore pressure, thereby reducing the effective stress on the skeletal matrix along the failure plane, decreasing grain-to-grain friction and effective shear strength. Meanwhile, the loading by the weight of the water in the matrix increases the gravitational driving force [Saar and Manga, 2003; Schmidt and Bürgmann, 2003].

Our data show that the sliding motion tends to initiate shortly after the autumn rains begin in October or November (roughly when the 30-day accumulated precipitation total exceeds 300 mm), normally one to three months ahead of the arrival of the precipitation peak (red arrows). The gaps between the precipitation peak and the midpoint of sliding acceleration are typically within two months (blue arrows). Slope movement is triggered when the shear stress exceeds shear strength.

Phenomena other than sliding also affect ground movement. During a dry season, the soil-material matrix undergoes stress release and poroelastic rebound as the soil dries during the summer and early autumn, causing a slight regional uplift, which is similar to post-glacial or isostatic rebound [e.g., Cossart et al., 2014]. In addition, GPS can detect transient near-surface mass loading by precipitation, which contributes to seasonal vertical ground oscillation in wet regions of Washington and Oregon [Fu et al., 2015]. In particular, the elastic deformation of the ground in mountainous areas (e.g., the Cascade Range) occurs with larger amplitudes than in valley/basin areas. This is because the total precipitation accumulated during the wet seasons in the mountains at higher elevation is larger than that in the valleys/basins at lower elevation. This phenomenon can be seen at GPS station P429 (green benchmark in Fig. 1 B) at Cascade Locks across the river from the landslide complex. Assuming that the positioning data of P429 exhibit the same regional movement as the landslide study area, we derived the slope-parallel movement from GPS measurements at each SAR acquisition date using the same geometry parameters of location *P* that applied to InSAR results (Fig. 10 A). The non-linear component of GPS-derived slope-parallel movement was superposed on the continuous low-pass filtered vertical movement measured by GPS, and was compared with the precipitation records (Fig. 10 B). As expected, the GPS-derived seasonal slope-parallel oscillations are mainly dependent on the vertical movement (gray line in Fig. 10 B) as shown by being in phase. Both measurements derived from GPS and InSAR data depict a lower-than-average seasonal oscillation in 2010, as would be expected in a drought year [Fu et al., 2015] with lower-than-average precipitation totals. In addition, we also found that the InSAR and GPS results show fluctuations that are in phase and at similar frequency. However, the magnitude of InSAR-derived non-linear peak-to-trough slope-parallel movement (~120 mm) on the slide body is four times as large as that of off-slide GPS site (~30 mm). Inspired by the mechanism of the motion magnitude difference in mountainous and valley/basin areas [Fu et al., 2015], the exaggeration of the fluctuation magnitude on the landslide body can be explained by the fact that the GPS station at Cascade Locks site is next to the river (reservoir pool) and there is very little capacity for changes of near-surface water storage under the condition of high water table; however, the landslide body has a much thicker unsaturated zone, and thus more capacity to soak up water in the winter, indicative of a magnified hydrological loading effect. The only measurements of landslide thickness are from exploratory drilling by the U.S. Army Corps of Engineers on the lower part of the Bonneville landslide [Palmer, 1977]; thickness averaged about 75 m [Pierson et al., 2016]. However, the thickness of the other landslide bodies is not known

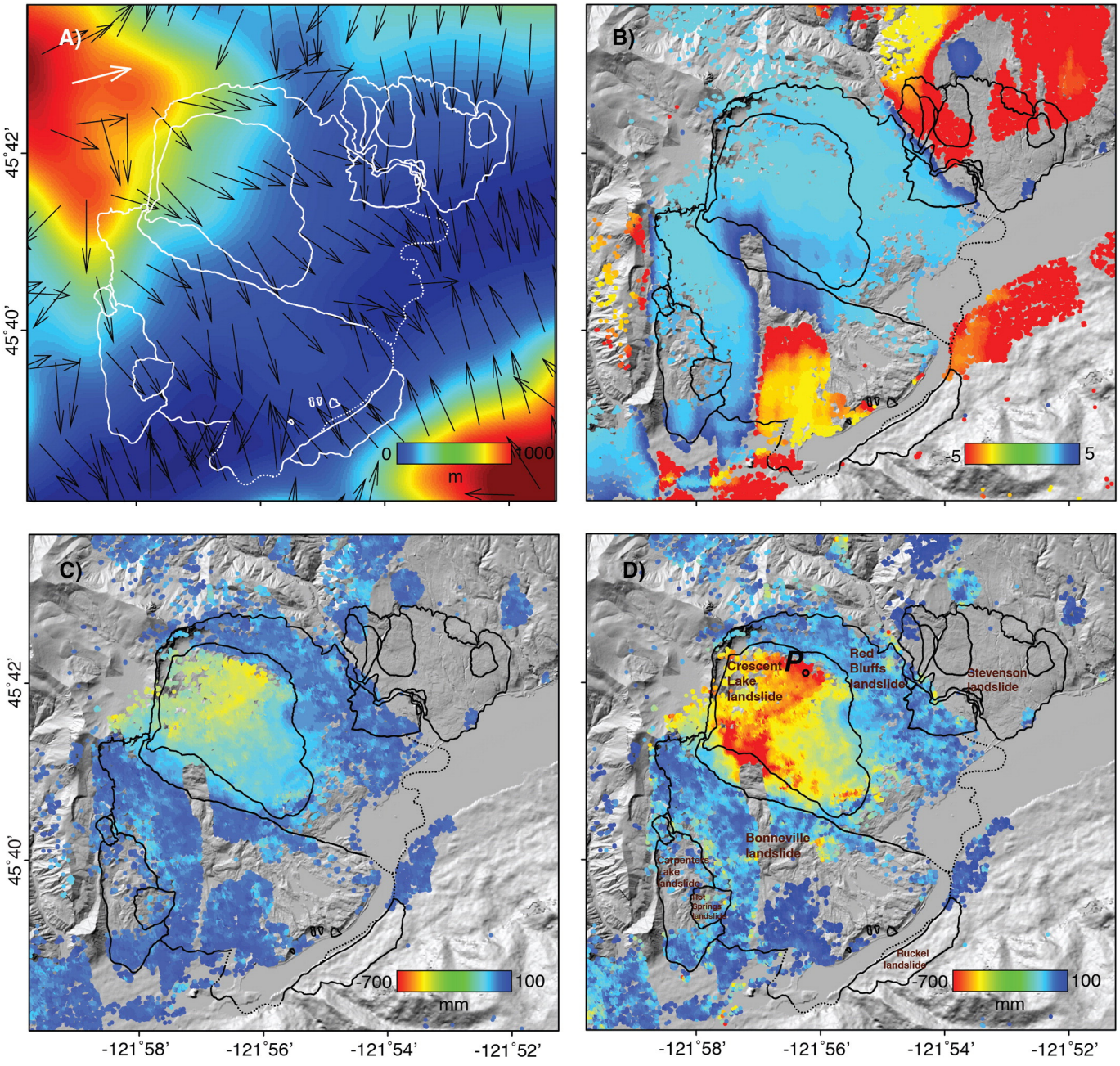

Fig. 8. Derived slope-parallel landslide motion in the study area. (A) Slope aspects (black arrows) superposed on topography with landslide boundaries delineated by white lines. The color scale shows the elevation in meters. The white arrow on the top left corner represents radar look vector, which is nearly constant for all scatterers in the study area. (B) Amplification factor *A* for each CT point of P218 dataset. The color scale shows the value of amplification. Only coherent targets with amplification from −5 to 5 are plotted. Cumulative apparent LOS movement (C) and cumulative slope-parallel movement (D) from 2007 to 2011. The color scales of C and D show the movement in millimeters with stable areas shown in color blue. *P* is a location with active movement that is used in the analysis. (For interpretation of the references to color in this figure legend, the reader is referred to the web version of this article.)

except for a few places on the Stevenson landslide complex, where it is less [Pierson et al., 2016].

4. Discussion

InSAR is a powerful tool to detect active landslides and to explore the timing and magnitude of their motion, even in forested terrain. Satellite passes are now sufficiently frequent and the resolution is sufficiently high to allow time-series analyses of movements as small as tens of millimeters for active landslides. Furthermore, such analyses can reveal relationships between triggering precipitation and slide kinematics (the onset and termination of sliding motion and movement rates).

To analyze the slide motion in response to rainfall, the de-trended InSAR-derived measurements were compared with the precipitation data, which were treated as a moving 30-day accumulation total. The beginning of subsiding vertical ground motion (black triangles in Fig. 9 B) gives the approximate (earliest possible) start of sliding motion, and we found that motion began when the 30-day accumulated precipitation total exceeded 300 mm. The gaps between the start of the sliding motion and the precipitation peak are generally less than three months. In particular, the drought year 2010 had the most variable precipitation with four 30-day peak totals between 300 and 400 mm spread over half a year, and slide motion repeatedly started and stopped. Total rainfall for the winter of 2010–2011 was also the least compared with that of the other years (~500 mm). This phenomenon appears to be reflected

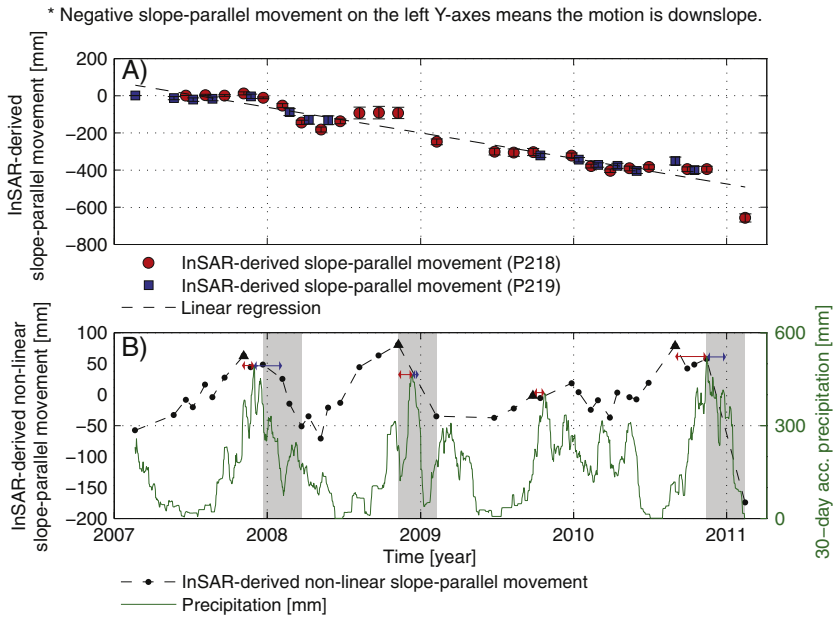

Fig. 9. Time-series InSAR-derived and GPS-derived slope-parallel ground motion correlating with 30-day accumulated precipitation total. (A) InSAR-derived slope-parallel movement at location *P* (shown in Fig. 8 D) on the active Crescent Lake landslide. All CT points within 100 m w.r.t. location *P* are considered in the calculation, and their averaged phase values are used for the integration of time-series deformation by P218 (red circles) and P219 (blue squares) using singular value decomposition (SVD). The error bars represent the standard deviation (up to 33 mm) of the measurements at the selected CT points. The linear regression showing the averaged movement rate is denoted with black dashed line (same to Fig. 10 A). (B) InSAR-derived non-linear slope-parallel movement (black dashed line) compared with the precipitation records (green line). To investigate the slide motion in response to the start of rainfall season as well as rainfall volume, the residual movement (black circles) after the removal of linear component (using left Y axis from −200 to 100 mm) and the 30-day accumulated precipitation total (using right Y axis from 0 to 600 mm) have been plotted together (same to Fig. 10 B). Black triangles depict the initiation of downslope motion, red arrows show the gaps between the initiation of downslope motion and the precipitation peak, gray bars indicate the sliding acceleration timespan that can be determined by the existing measurements, in which higher data sampling rate contributes to narrower bars and more precise estimation, and blue arrows show the gaps between the precipitation peak and the midpoint of sliding acceleration (same to Fig. 10 B). (For interpretation of the references to color in this figure legend, the reader is referred to the web version of this article.)

in the movement derived from both InSAR and GPS measurements, which show the smallest amount of movement of the observation period. Although we lack InSAR data for most of 2011, the year with the highest total precipitation, we have shown that the most active upper part of the Crescent Lake landslide experienced almost 300 mm of slope-parallel movement during the three-month period from November 2010 through January 2011.

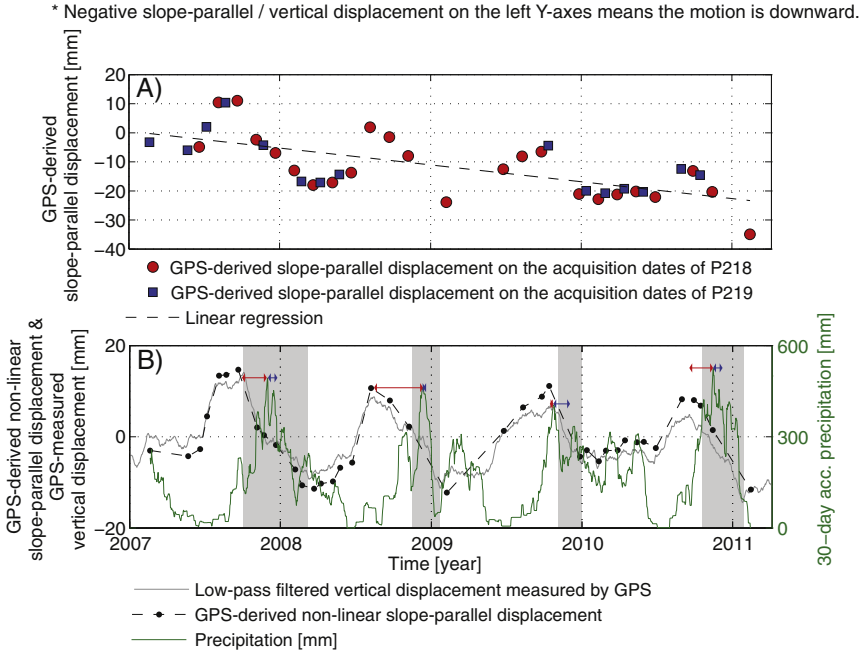

Fig. 10. (A) Regional movement of a nearby GPS station unaffected by landslides is projected into the slope-parallel direction at *P* to reflect the regional movement component along the slope at this location. (B) GPS-derived non-linear slope-parallel movement (black dashed lines) superposed on the low-pass filtered vertical deformation (gray line), and compared with the 30-day accumulated precipitation total (green line). The difference between this plot and the one in 9 B is that the initiation of downslope motion (black triangles) and the sliding acceleration timespan (gray bars) are determined by the vertical movement measured by GPS, rather than by the non-linear slope-parallel movement obtained from InSAR. (For interpretation of the references to color in this figure legend, the reader is referred to the web version of this article.)

GPS observations at a relatively stable site in Cascade Locks, Oregon have shown that measurement of landslide motion is complicated by regional seasonal ground oscillation due to mass loading by precipitation over Washington and Oregon. The oscillation frequency at Cascade Locks is similar to but smaller in magnitude than the variations in the InSAR-derived movement at the active slide body, suggesting higher capacity for hydrological loading on the thick and porous landslide body than at the lower terrain near the river.

An unexpected result of the InSAR analysis was that we detected approximately 300 mm of southeastward movement along the slope of a >0.8 km^2 block of terrain at the mouth of Greenleaf Basin between 2007 and 2011. This block is composed primarily of in-place bedrock that is immediately upslope of the ~150-m-high headscarps of the Bonneville and Red Bluffs landslides, and it was the source area for the 2008 rock avalanche.

The headscarp area of 2008 Greenleaf Basin rock avalanche is completely decorrelated so that InSAR is incapable of revealing the process of this specific avalanche. Nevertheless, an abrupt decrease of amplitude indicates that early incipient motion began between November 23, 2007 and December 22, 2007 prior to release of the Greenleaf Basin rock avalanche. Although loading by the Greenleaf Basin rock avalanche deposit (375,500 m^3) contributed new mass to the head of the Crescent Lake landslide (0.058% of the volume of the Crescent Lake landslide (6×10^8 m^3) [Randall, 2012], no evidence from our time-series deformation measurements suggests that the rock avalanche, which occurred during our monitoring period, affected the overall sliding motion.

Airborne repeat-pass of Uninhabited Aerial Vehicle Synthetic Aperture Radar (UAVSAR) and the newly launched (2014) ALOS PALSAR-2 satellite are collecting more L-band SAR imagery for mapping geohazards. In a future study, we plan to constrain the slide thickness and rheological parameters over the active Crescent Lake landslide using the complete 3D surface deformation [Delbridge et al., 2016] obtained from geodetic measurements (multi-spaceborne SAR and GPS observations).

5. Conclusions

This study demonstrates the usefulness of InSAR imagery to (1) detect cm-scale creeping motion of active, low-angle landslides in forested terrain; (2) determine the seasonality of landslide motion; and (3) correlate slide motion with the timing and magnitude of seasonal rainfall and with the isostatic effects of accumulated rainfall. In the study we evaluated ground motion at three locations within or adjacent to the Cascade landslide complex.

First, we evaluated the physical extent, timing, and magnitude of the 8-km^2 Crescent Lake landslide, a reactivated part of the larger Red Bluffs landslide. We cross-validated the time-series ground deformation using two independent and overlapping tracks of SAR datasets. Results showed that the central upper part of the landslide moved a total of 700 mm downslope during the 4-year observation period from 2007 to 2011 (more than the lower part of the landslide). Landslide movement was seasonal and showed a strong correlation with winter precipitation (running 30-day accumulated total). Downslope movement was separated (using nearby GPS measurements) from accompanying smaller-scale seasonal movement of the soil mantle caused by the mass-loading and shrink/swell effects by accumulated winter rainfall.

Second, we detected incipient motion on part of the headscarp of the Bonneville landslide more than a month prior to complete failure of this rock mass, which produced the 2008 Greenleaf Basin rock avalanche. Detection was accomplished by integrating two overlapping ALOS PALSAR-1 datasets and tracking the time-series amplitude values of selected targets with high DA values.

Third, we demonstrated that a 0.8-km^2-block of terrain upslope of the Bonneville and Red Bluffs landslide headscarps crept about 300 mm downslope in a southeastward direction over the four-year window of observation of this study. With movement possibly involving as much as 100 million m^3 of rock, this finding has significant downslope hazard implications.

Importantly, this study has demonstrated that L-band SAR imagery is readily capable of detecting low displacement-angle motion of landslides in forested terrain. The enrichment of SAR imagery archives and the development of SAR techniques are opening a new era for landslide monitoring, and will allow us to improve our understanding of landslide behavior and the mitigation of landslide risks.

Acknowledgement

We thank Washington Department of Natural Resources, Western Regional Climate Center, Desert Research Institute and UNAVCO for providing the LIDAR DEM, precipitation records and GPS observations, respectively. ALOS PALSAR-1 data acquired by Japan Aerospace Exploration Agency (JAXA) were distributed through Alaska Satellite Facility (ASF). This research was financially supported by NASA Earth and Space Science Fellowship (NNX15AN10H), U.S. Geological Survey (G14AC00153), and the Shuler-Foscue Endowment at Southern Methodist University. The geocoded maps were generated by the General Mapping Tools (GMT) and ArcGIS.

References

Berardino, P., Fornaro, G., Lanari, R., Sansosti, E., 2002. A new algorithm for surface deformation monitoring based on small baseline differential SAR interferograms. IEEE Trans. Geosci. Remote Sens. 40, 2375–2383.

Calabro, M.D., Schmidt, D.A., Roering, J.J., 2010. An examination of seasonal deformation at the Portuguese Bend landslide, southern California, using radar interferometry. J. Geophys. Res. 115 (F2).

Cannon, S.H., Kirkhamb, R.M., Parise, M., 2001. Wildfire-related debris-flow initiation processes, Storm King Mountain, Colorado. Geomorphology 39 (3–4), 171–188.

Chen, C.W., Zebker, H.A., 2001. Two-dimensional phase unwrapping with use of statistical models for cost functions in nonlinear optimization. J. Opt. Soc. Am. A 18 (2), 338–351.

Cossart, E., Mercier, D., Decaulne, A., Feuillet, T., Jónsson, H.P., Sæmundsson, P., 2014. Impacts of post-glacial rebound on landslidespatial distribution at a regional scale in northern Iceland (Skagafjörður). Earth Surf. Process. Land. 39, 336–350.

Delbridge, B.G., Bürgmann, R., Fielding, E., Hensley, S., Schulz, W.H., 2016. Three-dimensional surface deformation derived from airborne interferometric UAVSAR: application to the Slumgullion Landslide. J. Geophys. Res. Solid Earth 121 http://dx.doi.org/10.1002/2015JB012559.

DNR, 2005. LIDAR DEM of Skamania County. Washington Department of Natural Resources, Olympia Washington www.dnr.wa.gov.

Ferretti, A., Prati, C., Rocca, F., 2001. Permanent scatterers in SAR interferometry. IEEE Trans. Geosci. Remote Sens. 39 (1), 8–20.

Fu, Y., Argus, D.F., Landerer, F.W., 2015. GPS as an independent measurement to estimate terrestrial water storage variations in Washington and Oregon. J. Geophys. Res. Solid Earth 120, 552–566. http://dx.doi.org/10.1002/2014JB011415.

Gili, J.A., Corominas, J., Rius, J., 2000. Using global positioning system techniques in landslide monitoring. Eng. Geol. 55 (3), 167–192.

Handwerger, A.L., Roering, J.J., Schmidt, D.A., Rempel, A.W., 2015. Kinematics of earthflows in the Northern California Coast Ranges using satellite interferometry. Geomorphology 246, 321–333.

Highland, L.M., Bobrowsky, P., 2008. The landslide handbook–a guide to understanding landslides. U.S. Geol. Surv. Circ. 1325, 129.

Hilley, G.E., Bürgmann, R., Ferretti, A., Novali, F., Rocca, F., 2004. Dynamics of slow-moving landslides from permanent scatterer analysis. Science 304 (5679), 1952–1955. http://dx.doi.org/10.1126/science.1098821.

Hooper, A., 2010. A Statistical-Cost Approach to Unwrapping the Phase of Insar Time Series. European Space Agency Special Publication ESA SP-677.

Iverson, R.M., 2000. Landslide triggering by rain infiltration. Water Resour. Res. 36 (7), 1897–1910.

Iverson, R.M., George, D.L., Allstadt, K., Reid, M.E., Collins, B.D., Vallance, J.W., Schilling, S.P., Godt, J.W., Cannon, C.M., Magirl, C.S., Baum, R.L., Coe, J.A., Schulz, W.H., Bower, J.B., 2015. Landslide mobility and hazards: implications of the 2014 Oso disaster. Earth Planet. Sci. Lett. 412, 197–208.

Kargel, J.S., Leonard, G.J., Shugar, D.H., Haritashya, U.K., Bevington, A., et al., 2016. Geomorphic and geologic controls of geohazards induced by Nepal's 2015 Gorkha earthquake. Science 351 (6269). http://dx.doi.org/10.1126/science.aac8353.

Kim, J.W., Lu, Z., Qu, F., Hu, X., 2015. Pre-2014 mudslides at Oso revealed by InSAR and multi-source DEM analysis. Geomat. Nat. Haz. Risk 6 (3), 184–194.

Lawrence, D.B., Lawrence, E.G., 1958. The bridge of the gods legend, its origin, history, and dating. Mazama 40 (13), 33–41.

Malamud, B., Turcotte, D., Guzzetti, F., Reichenbach, P., 2004. Landslides, earthquakes, and erosion. Earth Planet. Sci. Lett. 229. http://dx.doi.org/10.1016/j.epsl.2004.10.018.

O'Connor, J.E., 2004. The evolving landscape of the Columbia River Gorge–Lewis and Clark and cataclysms on the Columbia. Or. Hist. Q. 105 (3), 390–421.

O'Connor, J.E., Burns, S.F., 2009. Cataclysms and controversy–aspects of the geomorphology of the Columbia River Gorge. Geol. Soc. Am. Field Guides 2009 (15), 237–251.
Palmer, L., 1977. Large landslides of the Columbia River Gorge, Oregon and Washington. Rev. Eng. Geol. 3, 69–84.
Pierson, T.C., Lu, Z., 2009. InSAR detection of renewed movement of a large ancient landslide in the Columbia River Gorge, Washington. Geological Society of America Abstract with Programs, 2009 Portland Annual Meeting 41 (7), 497.
Pierson, T.C., Evarts, R.C., Bard, J.A., 2016. Landslides in the western Columbia Gorge, Skamania County, Washington. U.S. Geological Survey Scientific Investigations Map 3358.
Randall, J.R., 2012. Characterization of the Red Bluff Landslide, Greater Cascade Landslide Complex, Columbia River Gorge, Washington. Portland State University, Master Thesis.
Saar, M.O., Manga, M., 2003. Seismicity induced by seasonal groundwater recharge at Mt. Hood, Oregon. Earth Planet. Sci. Lett. 214, 605–618.
Samsonov, S., 2010. Topographic correction for ALOS PALSAR interferometry. IEEE Trans. Geosci. Remote Sens. 48 (7), 3020–3027.
Schmidt, D.A., Bürgmann, R., 2003. Time-dependent land uplift and subsidence in the Santa Clara valley, California, from a large interferometric Synthetic Aperture Radar data set. J. Geophys. Res. 108 (2416), B9. http://dx.doi.org/10.1029/2002JB002267.
Schmidt, D.A., Tong, X., 2015. A survey of landslide activity in the Columbia River Gorge from InSAR. American Geophysical Union (AGU) Annual Meeting. California, San Francisco.
Schulz, W.H., Kean, J.W., Wang, G., 2009. Landslide movement in Southwest Colorado triggered by atmospheric tides. Nat. Geosci. 2, 863–866. http://dx.doi.org/10.1038/NGEO659.
Simons, M., Rosen, P., 2007. Interferometric synthetic aperture radar geodes. In: Schubert, G. (Ed.), Treatise on Geophysics, Vol. 3, Geodesy. Elsevier, Amsterdam, pp. 391–446.
Tong, X., Schmidt, D.A., 2014. Investigating Persistent and Distributed Scatterers to better resolve low amplitude deformation with InSAR in vegetated terrains. Abstract G23B-0488 presented at 2014 Fall Meeting, AGU, San Francisco, Calif., 15–19 Dec.
Walsh, T.J., Korosec, M.A., Phillips, W.M., Logan, R.L., Schasse, H.W., 1987. Geologic map of Washington—Southwest quadrant. Washington Division of Geology and Earth Resources, Geologic Map GM–34, scale 1:250,000.
Wise, W.S., 1961. The Geology of the Wind River Area, Washington, and the Stability Relations of Celadonite. John Hopkins University, PhD Dissertation, pp. 191–195.
Zhao, C., Lu, Z., Zhang, Q., Fuente, J., 2012. Large-area landslide detection and monitoring with ALOS/PALSAR imagery data over Northern California and Southern Oregon, USA. Remote Sens. Environ. 124, 348–359.